ABSTRACT

Title of thesis: Dynamics and control of a soft segmented robot for underwater and terrestrial locomotion

Prateek Jaya Prakash
Master of Science, 2020

Thesis directed by: Professor Derek A. Paley
Department of Aerospace Engineering and
Institute for Systems Research

The thesis investigates the modeling and control a of bio-inspired soft-segmented robot in underwater and terrestrial domains. Animals have evolved to navigate through complicated environments and perform tasks. Soft-bodied animals excel at manipulation in tight environments and are the inspiration for the growing research in soft robotics. With benefits including reduced weight and design complexity as compared to rigid robots, a soft segmented robot is a viable design alternative. This work explores the mathematical modeling methodology, dynamics, and control of a soft segmented robot in underwater and terrestrial domains. Planar discrete elastic rod (PDER) theory is used to model the soft-robot and simplified fluid force and friction force models are used to describe the influence of the environment. The PDER framework produces a state-space description of the dynamics that is amenable to feedback control design, as well as computationally efficient. The feedback control law is based on a decentralized control algorithm that aims to minimize the sensing and communication requirements in practice.

Dynamics and control of a soft segmented robot for underwater and terrestrial locomotion

by

Prateek Jaya Prakash

Thesis submitted to the Faculty of the Graduate School of the
University of Maryland, College Park in partial fulfillment
of the requirements for the degree of
Master of Science
2020

Advisory Committee:
Dr. Derek A. Paley, Chair/Advisor
Dr. Mumu Xu
Dr. Nikhil Chopra

Dedication

I dedicate this work to my parents, Jayaprakash S. and Rupa K. S., who have supported me in all my ventures, and to whom I owe everything in my life.

Acknowledgments

I owe my gratitude to all the people who have made this thesis possible and because of whom my graduate experience has been one that I will cherish forever.

First and foremost I'd like to thank my advisor, Dr. Derek Paley for giving me an invaluable opportunity to work on this challenging and extremely interesting project over the past year. He has always made himself available for help and advice and provided me with useful suggestions, without which this thesis would not have been possible. It has been a pleasure to have been a part of the Cooperative Dynamics and Control Lab, a research community that has inspired me and my work over the last year. I would also like to thank Dr. Mumu Xu and Dr. Nikhil Chopra for agreeing to serve as members of my thesis committee.

I would like to thank my colleague, Dr. Will Scott. Without his extraordinary theoretical ideas and computational expertise, this thesis would have been a distant dream. It has been a genuine pleasure to have collaborated with him over the last year and will continue to look up to his work for inspiration.

I owe my deepest thanks to my family- my mother and father for their support and faith in me and for motivating me to follow my dreams. I would also like to mention my grandparents who have instilled in me, a sense of spirituality, which has brought balance to my life. I would like to express my gratitude to my friends for their unwavering support

and help through these troubling times. I am extremely grateful for having them in my life and extremely proud to call them family.

Music has always been a form of therapy to me. I express my gratitude to the late great Leonard Cohen, the amazing Damien Rice and the band Kodaline for their timeless music which has helped me gain perspective during troubled times.

It is impossible to remember all, and I apologize to those I've inadvertently left out.

Lastly, thank you all and thank God!

Table of Contents

List of Tables

List of Figures

List of Abbreviations

Chapter 1: Introduction

1.1 Motivation

Robotics represents the forefront of inter-disciplinary engineering and innovation. The last half century has seen a monumental rise in computational capabilities and consequently a burst of technological innovation that has led to robots being a part of everyday life. Yet until the recent decade, robotics research has been mostly restricted to rigid materials and convention actuation mechanisms. Soft robotics remains relatively unexplored with potential for game-changing ideas.

The main challenges of using soft or flexible materials are their non linearity and the need for a computationally viable continuum model to analyze these non linear dynamics. Further, these hyper-elastic materials need to produce large bending motions that are difficult to characterize. This in turn leads adds complexity to the control algorithms needed to perform tasks.

However, soft materials do have several advantages that simply cannot be mimicked by traditional materials. Soft materials are lightweight, affordable and can be easily customized. When coupled with fluidic actuation, they offer modular architectures that can be rapidly fabricated. Recent advancements in rapid manufacturing techniques has enabled the fabrication of parts with complex geometries, which in turn has contributed

to the growth in the popularity of soft robots.

Hence, from an engineering perspective, soft robots and, in particular, bio-inspired soft robots present a challenge that brings out the very best of inter-disciplinary research and creativity that is too good to pass up. This thesis explores the dynamics and control of such soft robots in underwater and terrestrial domains.

The next natural step is to look into the existing literature on soft robot locomotion.

1.2 Literature review

1.2.1 Bio-inspired soft robots

Bio-inspired robotics is a well-explored research domain. With potential for application in areas such as underwater rescue missions, equipment maintenance and surveillance [3], the last two decades has seen a significant rise in publications in this domain, especially in snake-like robots. The long and slender segmented structure of such robots provide superior capabilities for access through narrow openings and within confined areas [4].

In nature, evolution is driven by need and generally increases a species' chances of survival. We see a plethora of living creatures surviving in harsh climates across the globe each with their own physiological adaptations. Amongst these, many flaunt soft, flexible exoskeletons [5].

Though most models of snake-like robots view the structure as a discrete series of rigid links [6] a geometrically exact continuous model was investigated in [7]. A few examples of soft robotic snake-like robots exist, including a super-thin transparent

device based on dielectric elastomer actuators [8], and a fiber-reinforced fluidic actuator design [9]. Passive bending dynamics are found to aid locomotion of snakes over obstacle-filled terrain [10].

Segmented robots can be robust to mechanical failure because they are modular and highly redundant. On the other hand, one of the main drawbacks is their poor power efficiency for locomotion [4].

While soft actuators themselves are lightweight and flexible, they often require rigid or heavy electronic or mechanical components to provide power, including batteries, circuit boards, and pumps for fluidic actuators. For example, one soft snake-like robot [9] must include a large rigid head to house a fluid pressure source. Recent examples of advances in remote power delivery in soft robotics include wireless electric charging for a shape-memory alloy (SMA) caterpillar robot [11] and light-based energy delivery in a tensegrity rolling robot with liquid-crystal elastomer actuators [12]. In additional, chemical reactions have been utilized as a source for fluidic pressure in order to build an octopus robot out of entirely flexible materials [13].

The scope of this thesis is limited to virtual simulations of a soft segmented robot. Hence, the choice of actuation mechanism holds little influence over the nature of the control input to the system.

1.2.2 Undulating locomotion in soft robots

Due to the inherent non-holonomic constraint on wheels, existing snake-like robots [6] present a control design challenge that has led to the development of several novel

locomotion algorithms algorithms.

Early research in experimental biology [14] [15] studied several modes of locomotion in desert snakes and identified four common gaits: serpentine, side winding, concertina, and rectilinear. Fundamentally, the four gaits can be thought of variations of a wave-like motion moving though the body that is explored in chapter 2. Subsequently, further mechanical analysis helped [16] [17] quantify this travelling wave behaviour and develop empirical relationships between wave parameters and snake locomotion velocity.

The serpenoid-curve formulation of Hirose [18] states that the joint angles in a modular, snake-like terrestrial [19] or underwater [3, 20] robot vary sinusoidally in time using the same frequency and amplitude at each segment, with a constant phase difference between neighboring segments. Serpenoid trajectories have been applied to a variety of segmented robot morphologies over time, including wheeled and sliding designs on land [19] and snake-inspired underwater robots with rigid rotating joints [3, 20].

1.3 Thesis contributions

The primary contribution of this work is the mathematical model for feedback control of traveling-wave locomotion in underwater and terrestrial domains. The Planar Discrete Elastic Rod (PDER) framework results in an attractive and numerically efficient model that includes external forces and user inputs. A computationally tractable fluid force model is used to capture the influence of external environment. The proposed framework models both the added mass and inertial fluid forces acting on each soft segment in a fluid. (The work on underwater locomotion of soft segmented robot was previously published

as part of [2].)

The work on terrestrial locomotion incorporates a stick-slip friction model. Similar to the underwater case, the PDER framework is used to describe the dynamics of the system, now including frictional force from the stick-slip model. By modeling both static and dynamic friction, a computationally viable and physically accurate mathematical description of surface friction is proposed.

This work proposes a feedback-control algorithm based on a travelling wave to control the states of the soft segmented robot. An open-loop parameter study serves as the baseline against which the closed-loop performance is compared. The control strategy is decentralized, i.e, each segment can only interact with its neighboring nodes. Hence, the control law is computationally efficient, and impose fewer sensing and communication requirements that a centralized model.

The performance of the soft-segmented robot is dependent on various physical and control variables. An extensive parameter study is done to quantify the dependence of the performance metrics on these factors. This parameter study is intended to be used as a look-up table for future design changes or new developments in similar soft segmented robots.

1.4 Thesis organization

Chapter 2 of the thesis outlines the mathematical and conceptual background upon which the following chapters of the thesis are built. Chapter 3 introduces the control algorithm and procedure that serves the rest of the thesis. The concept of a travelling wave

is introduced here and the fundamentals of centralized and decentralized network control architectures are outlined.

Chapter 4 explores underwater locomotion. Concepts from Chapters 2 and 3 are used to develop the state space model of the snake-like robot. Open-loop dynamics are first analysed to construct a parameter study aimed at identifying the open-loop optimal performance region. Next, the centralized and the decentralized feedback control algorithms are implemented. Finally the performance of the closed loop system is compared to the open-loop system.

Chapter 5 explores terrestrial locomotion of soft segmented worm-like robots. It follows a similar structure as Chapter 4 in which we look at the open-loop dynamics of the system followed by the application of a decentralized feedback control algorithm to the system.

Chapter 6 summarizes the findings of the thesis and discusses the implications of the results. We also discuss possible future directions of work in this area.

Chapter 2: Dynamics of a soft segmented robot

This chapter presents a mathematical model for locomotion in a flexible underwater robot. The Planar Discrete Elastic Rod (PDER) formulation is used to describe the robot's state as a discrete series of nodes and edges, with internal forces arising from stretching and bending deformation. The external forces to the system are the fluid and frictional forces, which are discussed in detail later in the chapter. (The material in this chapter was previously published as part of [2].)

2.1 Bending and stretching of elastic rods

An elastic rod is a continuum structure with an infinite number of degrees of freedom. However, from the perspective of computation, this is far from ideal. A discrete model is a computationally tractable approach to the elastic-rod problem. The behavior of the elastic rod is suitably approximated using a planar discrete elastic rod formulation [1], which is a specialization of three-dimensional discrete elastic rod theory [21].

The Discrete Elastic Rod (DER) formulation by Bergou et al. [21] exploits concepts from discrete differential geometry resulting in an attractive and numerically efficient avenue to model the three-dimensional dynamics of elastic rods that are capable of bending, stretching and twisting. The advantages of using the DER model include generation of

ordinary differential equations for the motion of the soft robot that can interface with control schemes and contact algorithms, ability to incorporate a hierarchy of rod models, and ease of interpretation and measurement of kinematic quantities.

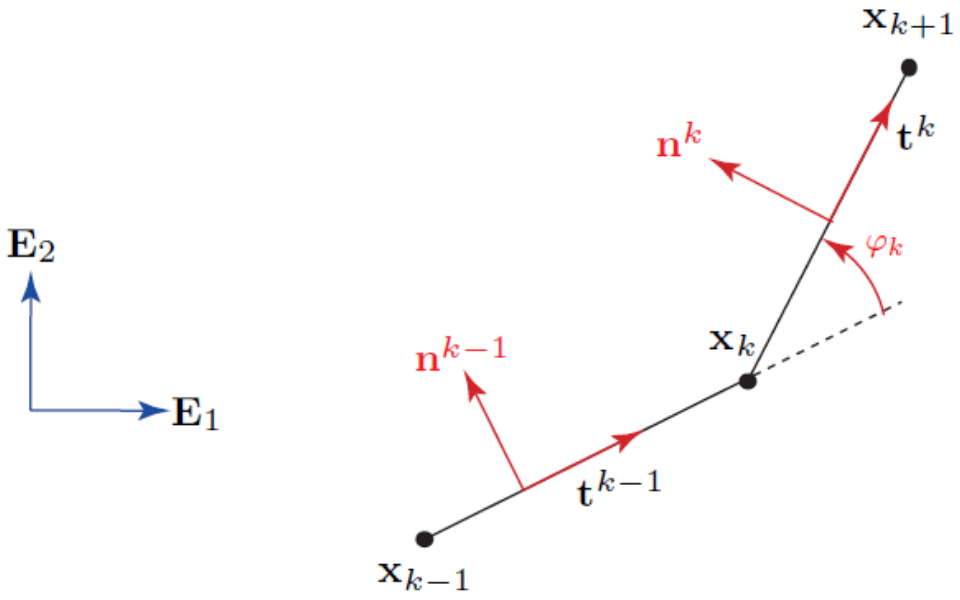

Figure 2.1: Notations used for labeling nodes and edges [1]

The rod is discretized into a series of N nodes connected by $N-1$ edges. The position of the k^{th} node is [1]

$$\boldsymbol{x}_k = x_k \boldsymbol{E}_1 + y_k \boldsymbol{E}_2, \tag{2.1}$$

where x_k and y_k are Cartesian coordinates, $\boldsymbol{E}_1$ is a unit vector in the horizontal direction, and $\boldsymbol{E}_2$ is a unit vector in the vertical direction. It follows that $\boldsymbol{E}_3 = \boldsymbol{E}_1 \times \boldsymbol{E}_2$ is directed out of the plane. Edge $\boldsymbol{e}^k$ connects nodes $\boldsymbol{x}_k$ and $\boldsymbol{x}_{k+1}$. (Note, edges are denoted with superscript indexing and nodes are denoted by subscript indexing.) We have [1]

$$\boldsymbol{e}^k = \boldsymbol{x}_{k+1} - \boldsymbol{x}_k, \quad \boldsymbol{t}^k = \frac{\boldsymbol{e}^k}{\left\|\boldsymbol{e}^k\right\|}, \text{ and } \boldsymbol{n}^k = \boldsymbol{E}_3 \times \boldsymbol{t}^k. \tag{2.2}$$

The vectors $\boldsymbol{t}^k$ and $\boldsymbol{n}^k$ are the unit tangent and unit normal of the k^{th} edge, respectively.

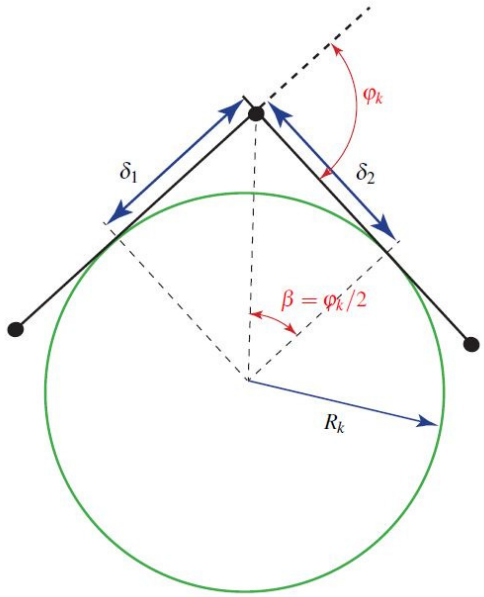

Figure 2.2: Curvature calculation at each node [1]

The discrete curvature at a node κ_i is defined as a function of the turning angle ϕ_k, where [1]

$$\begin{aligned} \varphi_k &= \cos^{-1}\left(\boldsymbol{t}^{k-1} \cdot \boldsymbol{t}^k\right), \\ \kappa_k &= \frac{2\sin(\phi_k)}{1+\cos(\phi_k)} = 2\tan\left(\frac{\phi_k}{2}\right), \end{aligned} \tag{2.3}$$

for $k = 1,...,N-2$, the internal nodes of the rod.

The intrinsic shape of a PDER is defined by the set of intrinsic lengths $\bar{l}^i$ of each edge and intrinsic curvatures $\bar{\kappa}_i$ at each node. This represents the resting or undeformed shape of the rod. Following Bergou et al. [21], the mass m_k associated with the k^{th} node

is the average mass of the edges meeting at this node, i.e.,

$$m_0 = \frac{1}{2} m^0 \tag{2.4}$$

$$m_k = \frac{1}{2}\left(m^k + m^{k-1}\right), \quad k = 1, \ldots, N-2 \tag{2.5}$$

$$m_{N-1} = \frac{1}{2} m^{N-2}. \tag{2.6}$$

The mass matrix M takes the form [1]

$$M = \begin{bmatrix} m_0 & 0 & \ldots & 0 & 0 \\ 0 & m_0 & \ldots & 0 & 0 \\ \vdots & \vdots & \ddots & \vdots & \vdots \\ 0 & 0 & \ldots & m_{N-1} & 0 \\ 0 & 0 & \ldots & 0 & m_{N-1} \end{bmatrix}. \tag{2.7}$$

Conservative elastic forces arising in the deformed rod are derived via scalar potential functions, where bending energy E_b is a function of the deviation between intrinsic and actual node curvatures and stretching energy E_s is a function of the deviation in length. The total elastic energy E_e is [1]

$$E_e = E_s + E_b, \tag{2.8}$$

where [1]

$$E_s = \frac{1}{2}\sum_{k=0}^{N-2} EA^k \left(\frac{\left\| \boldsymbol{e}^k \right\|}{\bar{l}^k} - 1 \right)^2 \bar{l}^k \tag{2.9}$$

$$E_b = \frac{1}{2}\sum_{j=1}^{N-2} \frac{EI_j}{\bar{l}_j} (\kappa_j - \bar{\kappa}_j)^2 \tag{2.10}$$

Here E is the elastic modulus of the rod, A^k is the cross-sectional area of the k^{th} edge, I_j is the area moment of inertia of the j^{th} node, and $\bar{l}_j = \frac{1}{2}(\left\| \boldsymbol{e}^j \right\| + \left\| \boldsymbol{e}^{j-1} \right\|)$ is the length of the Voronoi region of the j^{th} node. The area moment of inertia in the bending energy is based on the average area moment of inertia of neighboring edges, $I_j = \frac{1}{2}\left(I^j + I^{j-1} \right)$.

The conservative elastic force acting on node j is given by $F_{elastic,j} = -\partial E_e / \partial \mathbf{r}_j$ [21]. Stretching forces are tangent to the edges, whereas bending forces are normal to the edges. The force due to stretching at a node is a function of its own position, along with the positions of its nearest neighbor to either side, and the force due to bending at a node is a function of its two nearest neighbors to either side. The localized nature of the force computation gives the Jacobian matrix of the system a banded structure, which allows for the use of efficient numerical solvers [21]. Figure 2.3 illustrates the directions that forces act on the nodes due to stretching and bending deformation. For a full derivation of the force expressions, see [1].

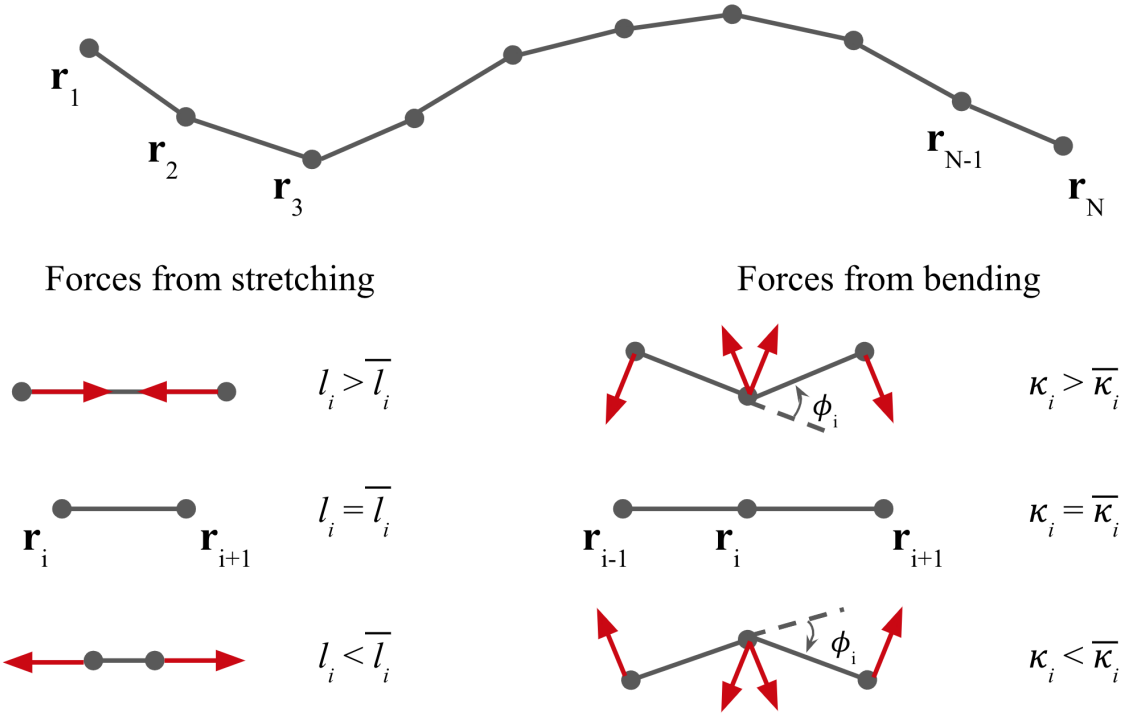

Figure 2.3: Illustration of the stretching and bending forces acting on each link [2]

2.2 State-space model of the elastic rod model

To write the dynamics in state-space form, let $\boldsymbol{q} = (x_1, y_1, \ldots, x_N, y_N)^T \in \mathbb{R}^{2N}$ represent the Cartesian coordinates of all of the nodes and $\boldsymbol{v} = (\dot{x}_1, \dot{y}_1, \ldots, \dot{x}_N, \dot{y}_N)^T \in \mathbb{R}^{2N}$ the node velocities. Let $\bar{\boldsymbol{\kappa}} \in \mathbb{R}^{N-2}$ be the vector of intrinsic curvatures of the interior nodes and $\bar{\boldsymbol{l}} \in \mathbb{R}^{N-1}$ the vector of intrinsic lengths of the edges.

The state-space model of the PDER is [21]

$$\begin{aligned}
\dot{\boldsymbol{q}} &= \boldsymbol{v} \\
\dot{\boldsymbol{v}} &= -M^{-1}\left(\frac{\partial E_t}{\partial \boldsymbol{q}} + \boldsymbol{F}_{ext}\right) \\
\dot{\bar{\boldsymbol{\kappa}}} &= B_\kappa \boldsymbol{u}_\kappa \\
\dot{\bar{\boldsymbol{l}}} &= B_l \boldsymbol{u}_l,
\end{aligned} \tag{2.11}$$

where $\boldsymbol{F}_{ext}$ is the column matrix containing the components of all external forces acting on the nodes, including the fluid and/or friction forces discussed in later sections. Consider two types of input to the system, corresponding separately to the stretching and bending motions. Input $\boldsymbol{u}_\kappa$ controls the rate of change of the intrinsic curvature, with matrix B_κ describing how the inputs are mapped to individual nodes, such that a single input may control curvature at many nodes, and a single node may be affected by multiple inputs. Similarly input $\boldsymbol{u}_l$ controls the rate of change of the intrinsic length of the edges, with matrix B_l describing which input maps to which edge. In the remainder of this thesis, we take B_k and B_l to be $N-2$ by $N-2$ identity matrix, such that each internal node ($i = 2, ..., N-1$) has a single unique bending/stretching input associated with it.

The elastic stretching and bending forces at each node are conservative and arise from the partial derivative with respect to $\boldsymbol{q}$ of the corresponding potential energy. (For an additional description of these forces refer to [22].)

2.2.1 Fluid force model

This section provides the framework for modeling hydrodynamic forces acting on a multi-link swimmer. Hydrodynamic forces induced by the motion of a body in an underwater environment are complex and nonlinear. For control design purposes, a simplified hydrodynamic model written in a closed form is preferred. Here, we use the model presented by Kelasidi et al. [23] to describe hydrodynamic forces in terms of the instantaneous velocities and accelerations of the edges in the PDER model. We choose our system parameters (see Table 4.1) to be similar to an rigid eel-like swimming robot, which operates with Reynolds number in the range 10^4 to 10^5 [23].

The proposed hydrodynamic model is based on Morison's equations [24] and models the forces between the fluid and the cylindrical links of underwater snake robots. The assumptions underlying the modelling approach are [23]:

1. The fluid is viscid, incompressible, and irrotational in the inertial frame.

2. The robot is neutrally buoyant, such that it operates in a horizontal plane within a volume of water.

3. The fluid is at rest in the inertial frame, such that there are no time-varying currents.

Fluid forces are calculated separately for each cylindrical link in the robot model [23], which here we associate with an edge in the PDER model. Let $\boldsymbol{v}^i = (\boldsymbol{v}_i + \boldsymbol{v}_{i+1})/2$ represent the velocity of edge i in the inertial frame. The scalar tangential and normal components of the i^{th} edge velocity are $v_t^i = \boldsymbol{v}^i \cdot \boldsymbol{t}^i$ and $v_n^i = \boldsymbol{v}^i \cdot \boldsymbol{n}^i$, respectively. Fluid drag forces are

calculated using separate drag coefficients, c_t for tangential and c_n for normal directions:

$$c_t = \frac{1}{4}\rho\pi C_f(a+b)l, \tag{2.12}$$

$$c_n = \rho C_D a l, \tag{2.13}$$

where a is the half-height and b is the half-width of the elliptical cross section of the robot and l is the length of the edge. Drag coefficients $C_f = 0.3$ and $C_d = 1.75$ come from studies of drag on a cylinder [23].

The fluid drag force acting on an edge $\boldsymbol{F}_D^i$ contains a linear term and a nonlinear quadratic term in each of the tangential and normal directions [23], i.e.,

$$\boldsymbol{F}_D^i = -c_t(v_t^i + v_t^i|v_t^i|)\boldsymbol{t}^i - c_n(v_n^i + v_n^i|v_n^i|)\boldsymbol{n}^i. \tag{2.14}$$

Additionally, the fluid force model includes an added mass term acting only in the normal direction,

$$\boldsymbol{F}_A^i = -\mu_n a_n^i = -\mu_n \dot{v}_n^i, \tag{2.15}$$

with coefficient $\mu_n = \rho\pi C_A a^2 l$ and added mass coefficient $C_A = 1.5$.

For the PDER model assume that the fluid forces acting on an edge are evenly distributed to the two nodes associated with the edge, such that the fluid force at each node

is

$$\begin{aligned}
\boldsymbol{F}_1^{fluid} &= \frac{1}{2}(\boldsymbol{F}_D^1 + \boldsymbol{F}_A^1), \\
\boldsymbol{F}_i^{fluid} &= \frac{1}{2}(\boldsymbol{F}_D^{i-1} + \boldsymbol{F}_A^{i-1} + \boldsymbol{F}_D^i + \boldsymbol{F}_A^i), \quad i = 2, ..., N-1, \\
\boldsymbol{F}_N^{fluid} &= \frac{1}{2}(\boldsymbol{F}_D^{N-1} + \boldsymbol{F}_A^{N-1}).
\end{aligned} \tag{2.16}$$

Although the fluid force model is idealized, the difference in drag coefficients for tangential and normal directions are sufficient to induce locomotion under a traveling wave gait, thus serving as a useful starting point for feedback control design in an underwater soft robot.

2.2.2 Friction force model

Developing a realistic model for frictional forces is tricky. Theoretically, the friction between two surfaces depends on several parameters like surface roughness, direction of relative motion, surface impurities, surface temperature, and so on. Hence, friction can rarely be modeled accurately and instead we try to understand friction as a function of known system parameters. The snake-like robot needs friction to perform locomotion. In the PDER model, the frictional force is included in the external force and is crucial for locomotion.

Broadly, there are two types of friction. Static friction is friction between two surfaces in contact that are not moving relative to each other. An object needs to overcome this resistance in order to move. For example, static friction is what prevents an object from sliding down an inclined surface. The static friction coefficient is represented by μ_{st}.

Kinetic friction on the other hand, occurs between two surfaces that are moving relative to each other. This dynamic friction results in a resistive force acting in a direction opposing the direction of movement. The dynamic friction coefficient is represented by μ_{dyn}.

The friction model to be adopted in this thesis is commonly referred to as the stick-slip friction model. The model transitions between static and dynamic friction based on a tolerance velocity (V_{tol}). In air, the normal force F_N on each link is constant and is the mass of the link times the acceleration due to gravity. The static and dynamic friction forces are

$$\boldsymbol{F}_{st} = \mu_{st}\boldsymbol{F}_N, \tag{2.17}$$

$$\boldsymbol{F}_{dyn} = \mu_{dyn}\boldsymbol{F}_N \tag{2.18}$$

Figure 2.4 is a flowchart representing the logic behind the stick-slip friction. A net force F_i is calculated based on the internal forces (F_{int}) and the frictional forces acting on the link and based on the instantaneous velocity of and internal forces acting on the link.

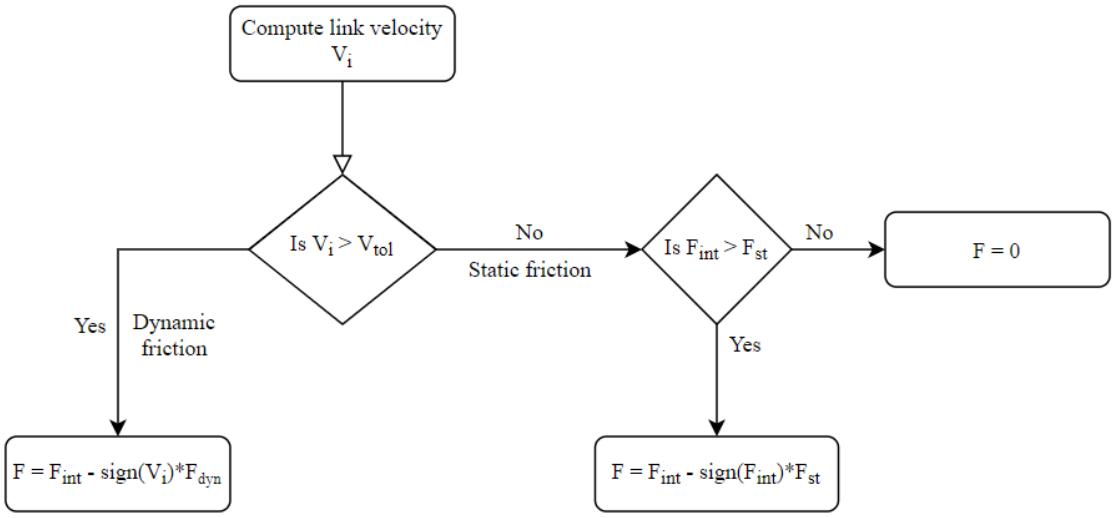

Figure 2.4: Overview of the friction force model

This frictional force is considered as an external force F_{ext} to the system. Hence, we can directly add these forces to the PDER state space model.

Chapter 3: Traveling wave locomotion with feedback control

This chapter builds on the state-space model developed in the previous section. During locomotion, the soft segmented robot transitions through different shapes or states. These states are driven by a sequence of actuator actions. The traveling wave motion is a popular mechanism to actuate segmented robots and is explored in this chapter. The material in this chapter was previously published as part of [2].

3.1 Traveling wave motion

Travelling-wave motion based on the serpenoid curve has been proposed to describe the shape of a snake or snake-like segmented robot in motion [18, 19], such that the angle between neighboring segments varies sinusoidally in time and in space (along the length of the body). The equation for the desired turning angle at node i includes amplitude α and turning bias γ parameters, along with a phase variable ψ_i associated with the node:

$$\phi_{i,des}(t) = \alpha \sin\left(\psi_i(t)\right) + \gamma. \tag{3.1}$$

Traveling-wave motion occurs when the phase angles increase linearly with time with frequency ω, while keeping the phase difference between neighboring nodes a constant

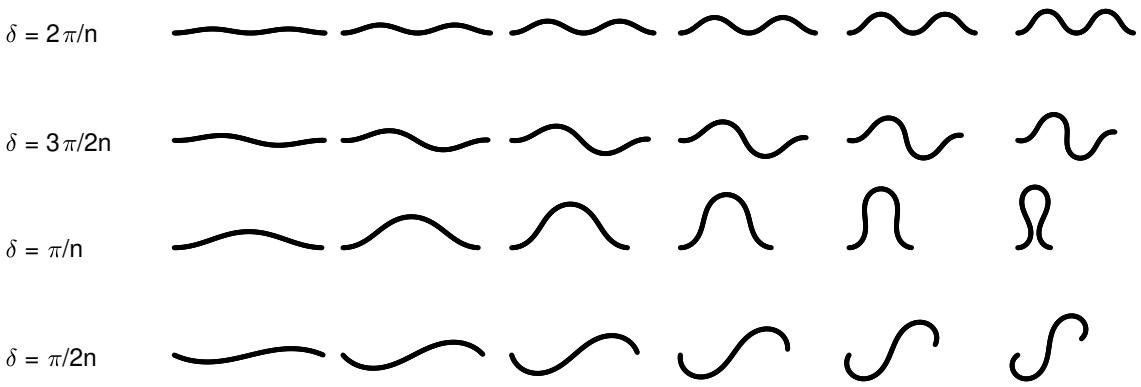

Figure 3.1: Illustrations of serpenoid curves described by (3.1) with $N = 100$ nodes [2]. Each row uses a different value of the phase offset δ, with amplitude α increasing from left to right.

value δ, i.e.,

$$\dot{\psi}_i = \omega, \tag{3.2}$$

$$\psi_i = \psi_{i-1} + \delta, \tag{3.3}$$

at every internal node $i = 2, ..., N - 1$.

Examples of serpenoid curves for a range of values of δ and α are illustrated in Fig. 3.1. For a given value of δ, there is a maximum amplitude α_{max} above which the curve will self-intersect.

To achieve a traveling-wave serpenoid motion given the phases ψ_i, the desired curvature and rate of change of curvature at each node are

$$\begin{aligned} \kappa_{i,des} &= 2 \tan\left(\frac{\alpha \sin\psi_i + \gamma}{2}\right), \\ \dot{\kappa}_{i,des} &= \alpha\dot{\psi}_i \cos\psi_i \sec^2\left(\frac{\alpha \sin\psi_i + \gamma}{2}\right). \end{aligned} \tag{3.4}$$

We consider several types of system architectures for determining the value of $\kappa_{i,des}(t)$. With a centralized approach, a pattern generator provides phase information to each node. Distributed approaches can achieve similar performance with fewer requirements on information transfer between nodes. We present a distributed controller wherein each node only needs to measure the curvature of its direct neighbor in order to estimate its proper phase over time. With that method, either the first node acts as the central pattern generator, or the first node is virtually connected to the last node to form a circulant topology to be fully decentralized.

3.2 Feedback control of bending and stretching

A feedback controller ensures that the actual curvature κ_i tracks the desired curvature $\kappa_{i,des}$ over time, given that the nodes have coordinated their phases based on a controller from Section 3.1. Assume that each node is able to measure its local curvature, rate of change of curvature, and intrinsic curvature, and optionally that nodes can share this information with one or more neighbors.

This section introduces a Proportional-Integral-Derivative (PID) control law that uses a measurement of the actual curvature κ_i at each node, as opposed to the controller of the previous section which measured only the intrinsic curvatures $\bar{\kappa}_i$. PID controllers are widely used and simple to implement due to the fact that they do not require a model of the system being controlled. The expression for the PID control input at each node is

$$u_i = \dot{\kappa}_{i,des}(t) + K_p e_i(t) + K_d \dot{e}_i(t) + K_i \int_0^t e_i(\tau) d\tau, \tag{3.5}$$

where $e_i = \kappa_{i,des} - \kappa_i$ is the error in actual curvature at node i. For numerical simulations, we choose $K_p = 10$, $K_d = 1$, and $K_i = 5$.

The individual gains can be tuned to achieve desired performance. Proportional gain K_p increases the speed of controller, but can lead to instability if taken too high. Derivative gain K_d serves to add damping to the system, which can remove unwanted oscillations at the cost of slowing down the dynamic response. The integral term with gain K_i serves to remove steady state errors.

To compare performance of the actual curvature feedback and intrinsic curvature tracking controllers, simulations were run using a range of values of amplitude α and frequency ω, using $\delta = 2\pi/(N-2)$, which gives a single full wave along the body. Parameter values for the simulations are summarized in Table 1. For the physical dimensions of the robot and corresponding fluid force coefficients, we use values from the rigid eel-like robot described in [4]. The elastic modulus $E = 1.875$ MPa is chosen to match that of Smoothsil 950 silicone rubber (Smooth-On, Inc.), which is commonly used to make bellows-style fluidic actuators [25]. We use $N = 10$ nodes in the PDER model, with eight intrinsic curvature rate inputs each associated with a single interior node.

Figure 4.1 illustrates the performance of the two controllers, in terms of average speed, deviation from desired curvature, and energy loss due to fluid drag forces. In general, for both controllers the speed increases with increasing frequency, and, for a given frequency, speed is maximized at a certain optimal amplitude with decreased speeds at higher and lower amplitudes. Frictional losses due to fluid drag forces increase monotonically with both amplitude and frequency. Figure 3.2 shows snapshots of the shape of the simulated robot over a single gait cycle, using two different amplitudes at the same

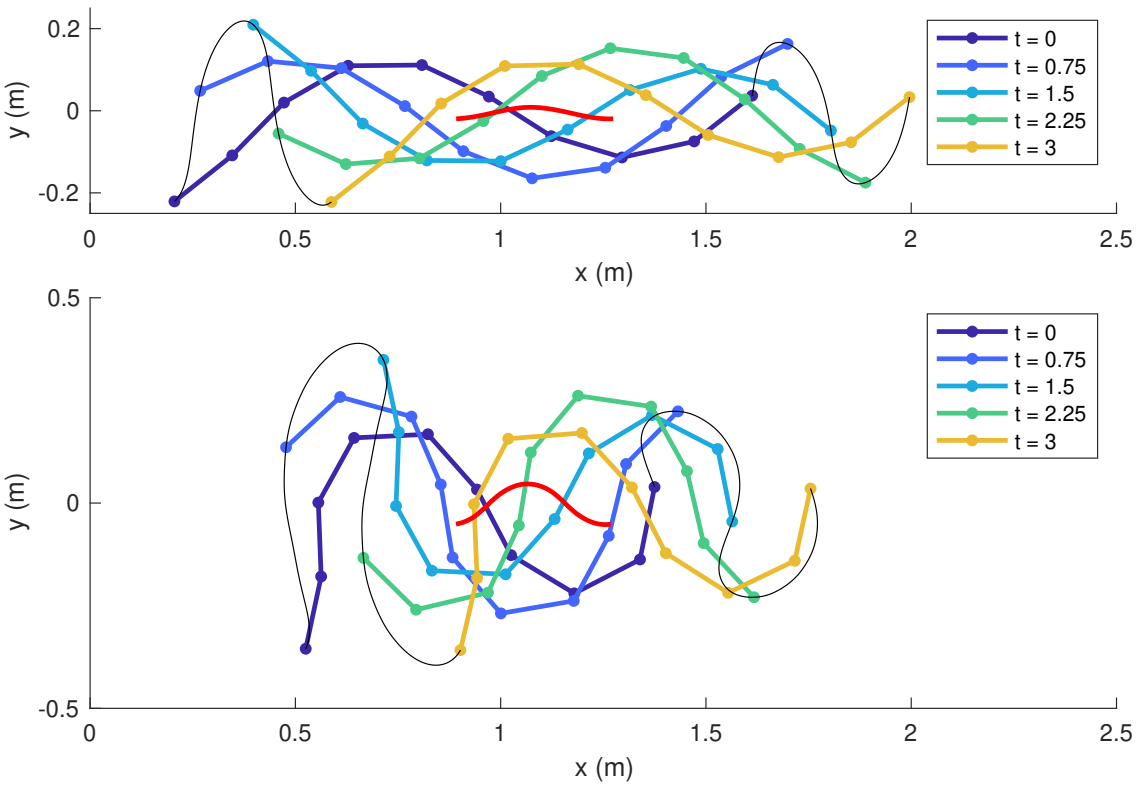

Figure 3.2: Snapshots of the simulated robot over a single cycle using the actual curvature feedback law, colored by time [2]. Top: $\alpha = \pi/6$, bottom: $\alpha = \pi/3$, both with $\omega = 2\pi/3$, and $\delta = \pi/4$. Black lines trace the trajectories of the first and last nodes, and the red line represents the motion of the center of mass.

frequency with actual curvature feedback control. Although the shapes traced out by the nodes are quite different in the two cases, the average speeds are within 2% (12.8 and 12.9 cm/s, respectively), whereas frictional losses are more than doubled at higher amplitude from 4.65 to 10.33 Watts.

3.2.1 Centralized control

The traveling wave phase constraints (3.2) can be achieved through a clock signal t, such that

$$\psi_i(t) = \omega t + \delta i + \psi_0, \tag{3.6}$$

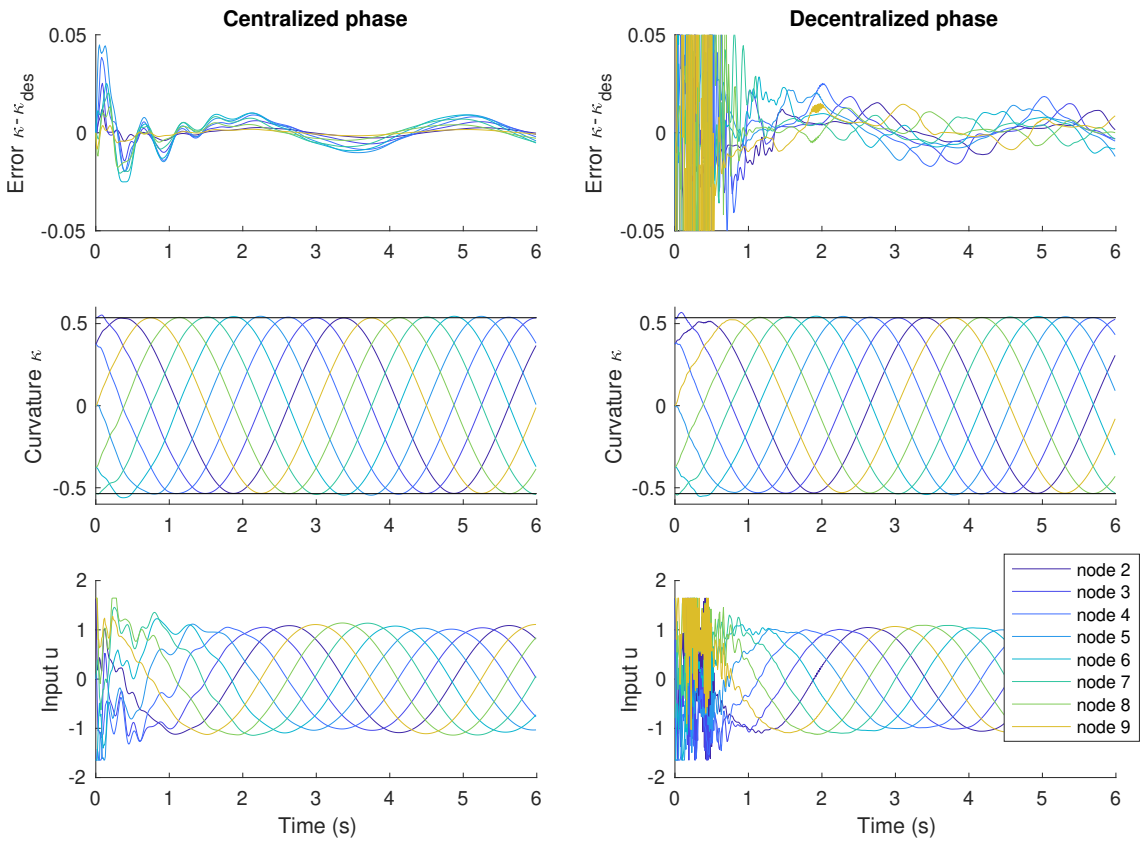

Figure 3.3: Comparison of centralized (left) and decentralized phase control (right) under the actual curvature feedback law, colored by node [2]. In both cases $\alpha = \pi/6$, $\omega = 2\pi/3$, and $\delta = \pi/4$ with PID gains $K_p = 10$, $K_d = 2$, $K_i = 1$. The top plots show the difference between actual curvature and desired curvature (as a function of phase) over time at each node. Middle plots show actual curvature, with black lines representing the nominal maximum value of $2\tan(\alpha/2)$. Bottom plots show the input u at each node, with saturation applied such that $|u_i| \leq 1.5\alpha\omega$.

for some arbitrary initial phase ψ_0. Note, the centralized approach corresponds to a hub and spoke communication architecture, where a central pattern generator sends the timing signal to each of the nodes. The next section describes a decentralized curvature-tracking control strategies to achieve the traveling wave using feedback.

3.2.2 Decentralized control

This section presents a decentralized controller for traveling wave motion where each node measures the curvature of its neighbor to estimate the current phase rather than relying on a central pattern generator. The estimated phase at each node is used to calculate the desired curvature and control input using the PID controller (5.2) from the previous section.

Suppose that each node can measure the curvature and rate of change of curvature of itself and its neighbors. If we assume that the curvature to vary sinusoidally, we can estimate the current phase at node i with

$$\hat{\psi}_i = 2(\phi_i,\ \dot{\phi}_i/\omega), \tag{3.7}$$

where turning angles and rates are calculated from the measured curvature and curvature rate:

$$\begin{aligned} \phi_i &= 2\tan^{-1}(\kappa_i/2), \\ \dot{\phi}_i &= \frac{4\dot{\kappa}_i}{\kappa_i^2 + 4}. \end{aligned} \tag{3.8}$$

We connect the nodes in a circulant topology, such that node i chooses its phase as an offset of the phase of its neighbor with index $i+1$, except for the last node $N-1$ which looks to node 2 to close the loop.

$$\psi_i = \hat{\psi}_{i+1} - \delta, \ i = 2, ..., N-2,$$

$$\psi_{N-1} = \hat{\psi}_2. \tag{3.9}$$

With this topology, information flows backward along the eel robot in the same direction as the traveling wave motion. This architecture has the advantage of not requiring an additional states in the system to represent the phase. Stability may be further improved through additional measurement filtering, which is the subject of ongoing work.

Figure 3.3 demonstrates that the performance of the decentralized phase control nearly matches that of the centralized phase. For both simulations, the robot starts at rest at $t = 0$ with curvatures equal to the desired curvature under the centralized phase control, with gait parameters $\alpha = \pi/6$, $\omega = 2\pi/3$, and $\delta = \pi/4$ and PID gains $K_p = 10$, $K_d = 2$, $K_i = 1$. Observe that for both cases, transient errors die out within one second, though errors in the decentralized case remain slightly higher in steady state. Larger oscillations exist in the decentralized case, with control becoming saturated initially at the prescribed maximum value of $|u_i| \leq 1.5\alpha\omega$.

Chapter 4: Undulatory locomotion in water

Locomotion underwater is inspired by aquatic snakes and eels, which exhibit an undulatory motion along their body. This wave-like motion is modeled based on the travelling wave equations described in Chapter 3. This results in the nodes oscillating at a given frequency and amplitude with successive phase difference between the nodes. Interactions with the fluid environment to produce locomotion. A simple open-loop simulation is enough to understand and quantify this movement. Figure 4.1 is a plot that traces the motion of the head, tail and body node of a soft, segmented robot in the inertial frame as the robot moves in the medium. Note that the robot moves from left to right in the figure.

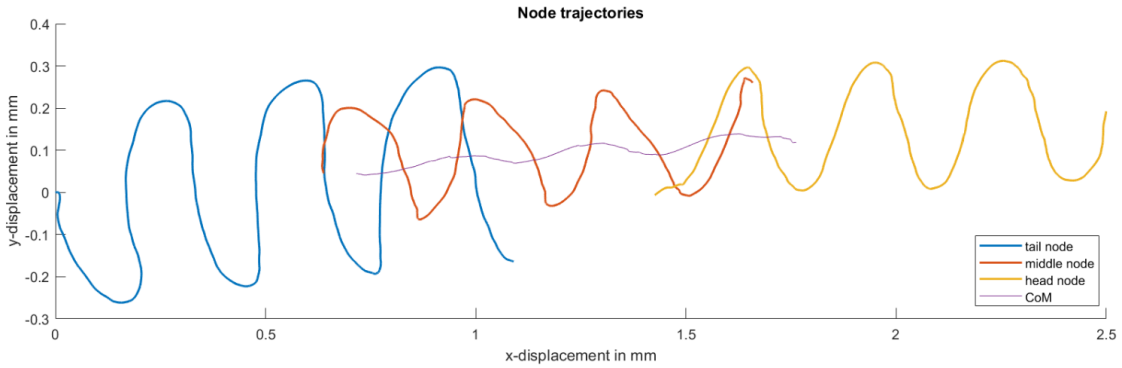

Figure 4.1: Trajectory of the nodes and the COM of the snake robot as it travels through the medium

4.1 Equations of motion

We combine the PDER state space model and the fluid force model from section 2 to arrive at the equations of motion that govern the dynamics of the snake-like robot.

$$\begin{aligned}
\dot{\boldsymbol{q}} &= \boldsymbol{v} \\
\dot{\boldsymbol{v}} &= -M^{-1}\left(\frac{\partial E_t}{\partial \boldsymbol{q}} + \boldsymbol{F}^{fl}\right) \\
\dot{\tilde{\boldsymbol{\kappa}}} &= B_\kappa \boldsymbol{u}_\kappa \\
\dot{\tilde{\boldsymbol{l}}} &= B_l \boldsymbol{u}_l,
\end{aligned} \tag{4.1}$$

where the fluid forces, $\boldsymbol{F}^{fl}$, are given by

$$\begin{aligned}
\boldsymbol{F}_1^{fl} &= \frac{1}{2}(\boldsymbol{F}_D^1 + \boldsymbol{F}_A^1), \\
\boldsymbol{F}_i^{fluid} &= \frac{1}{2}(\boldsymbol{F}_D^{i-1} + \boldsymbol{F}_A^{i-1} + \boldsymbol{F}_D^i + \boldsymbol{F}_A^i), \quad i = 2, ..., N-1, \\
\boldsymbol{F}_N^{fluid} &= \frac{1}{2}(\boldsymbol{F}_D^{N-1} + \boldsymbol{F}_A^{N-1}).
\end{aligned} \tag{4.2}$$

The controller in Section 4.3 is applied to the above state space model. It is important to note that rate of change of curvature is the input to the system.

4.2 Open-loop dynamics

This section describes the open-loop dynamics of the system 4.1–4.2. The objective of the analysis is to understand the behavior of the system and the quantify the influence

of parameters of interest.

In the simulation environment, various parameters have a direct effect on the performance of the system. These parameters and their values are listed in table 4.1. While simulating the system in the open-loop setting, the physical parameters of the system including the number of nodes, the number of inputs, the edge dimensions, and edge mass are fixed.

Name	Parameter	Value	Units
Number of nodes	N	10	
Number of bending inputs	N_u	8	
Time step	h	0.01	[s]
Edge length	$\bar{l}$	0.18	[m]
Edge mass	m	0.8	[kg]
Rod height	a	0.055	[m]
Rod width	b	0.05	[m]
Elastic modulus	E	1.875×10^6	[Pa]
Damping coefficient	d	0	
Water density	ρ	1000	$[\frac{\text{kg}}{\text{m}^3}]$
Drag coefficient	C_f	0.3	
Drag coefficient	C_D	1.75	
Added mass coefficient	C_A	1.5	
Inter-node phase difference	δ	$\pi/4$	[rad]

Table 4.1: Simulation parameter values. No units are provided for non-dimensional quantities.

The notable performance metrics of the open-loop simulation are the average speed, average curvature error and average power loss due to fluid friction. The simulation has three key factors: open-loop travelling wave amplitude, open-loop travelling wave frequency and the bending stiffness of the soft robot. Figure 4.2 is the input-output diagram for the same.

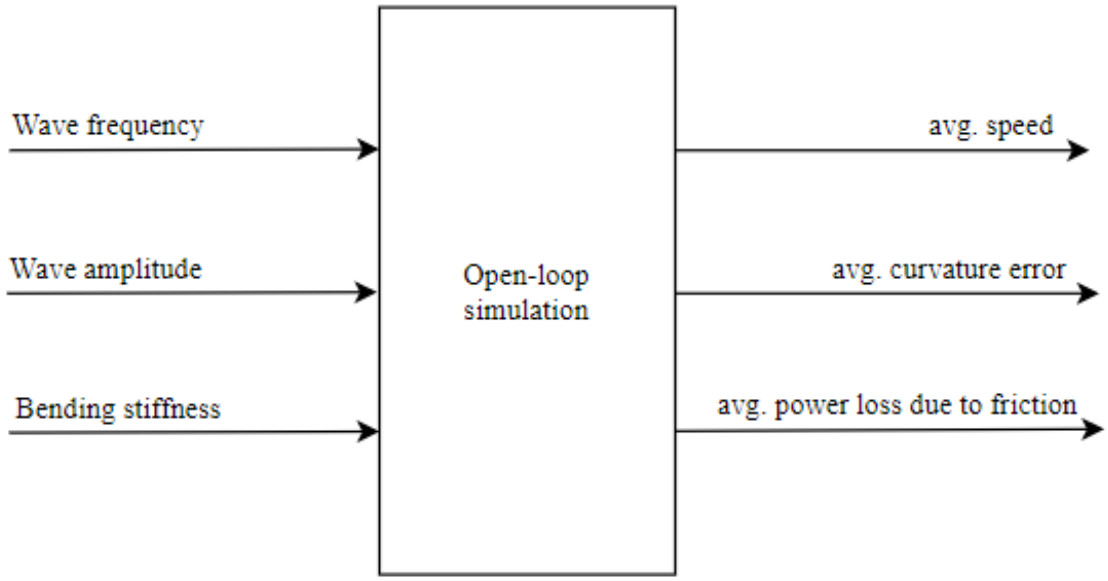

Figure 4.2: Open-loop simulation input output diagram

We now look at how each performance metric is affected by the individual factors and attempt to identify the region of optimal performance.

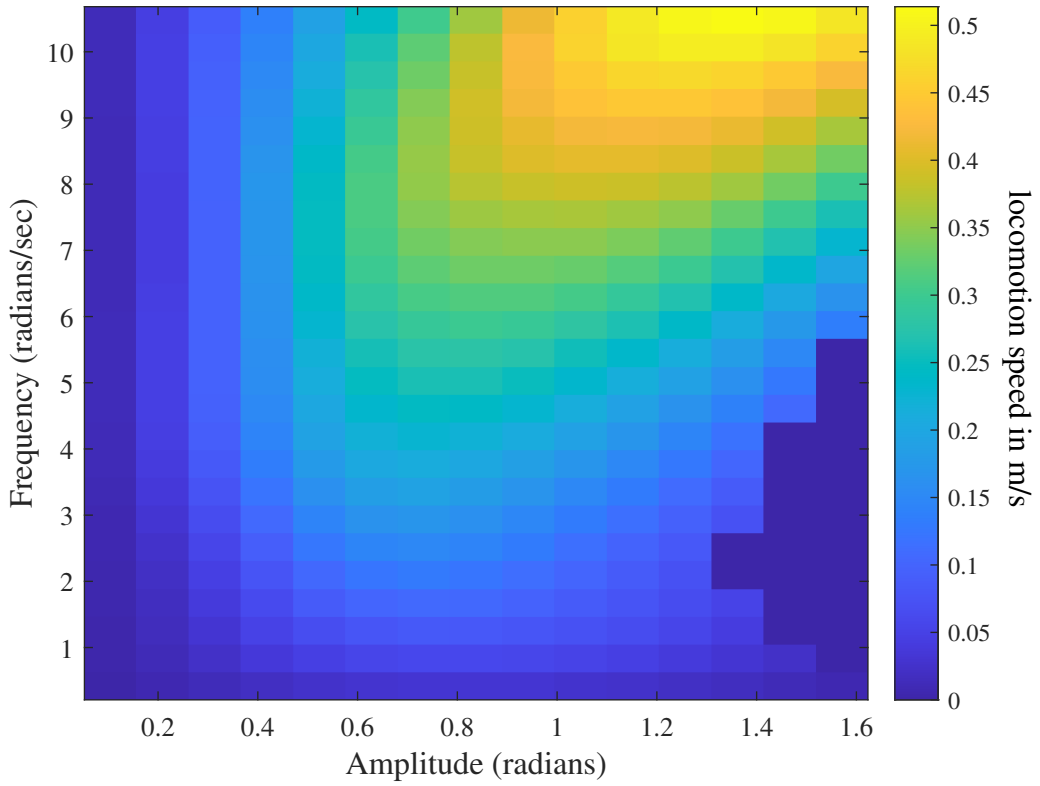

Figure 4.3: Open-loop average speed in m/s at a constant bending stiffness of $1.87\times10^4 Pa$

The open-loop controller is based on the travelling wave. The frequency and the amplitude of the travelling wave affect the performance of the robot. It is observed that the swimming speed is directly proportional to the amplitude and frequency. As long as we stay within the physical boundaries of the robot, a higher speed can be achieved at high values of frequency and/or amplitude. However, this gain in speed is coupled with significant drawbacks.

To understand these drawbacks, we look at curvature error and power loss due to friction. The average curvature error is defined as the accumulation of the difference between the actual and desired curvature at each time step. The power lost in interacting with the fluid environment is defined as the power lost to friction. From Figure 4.4, we

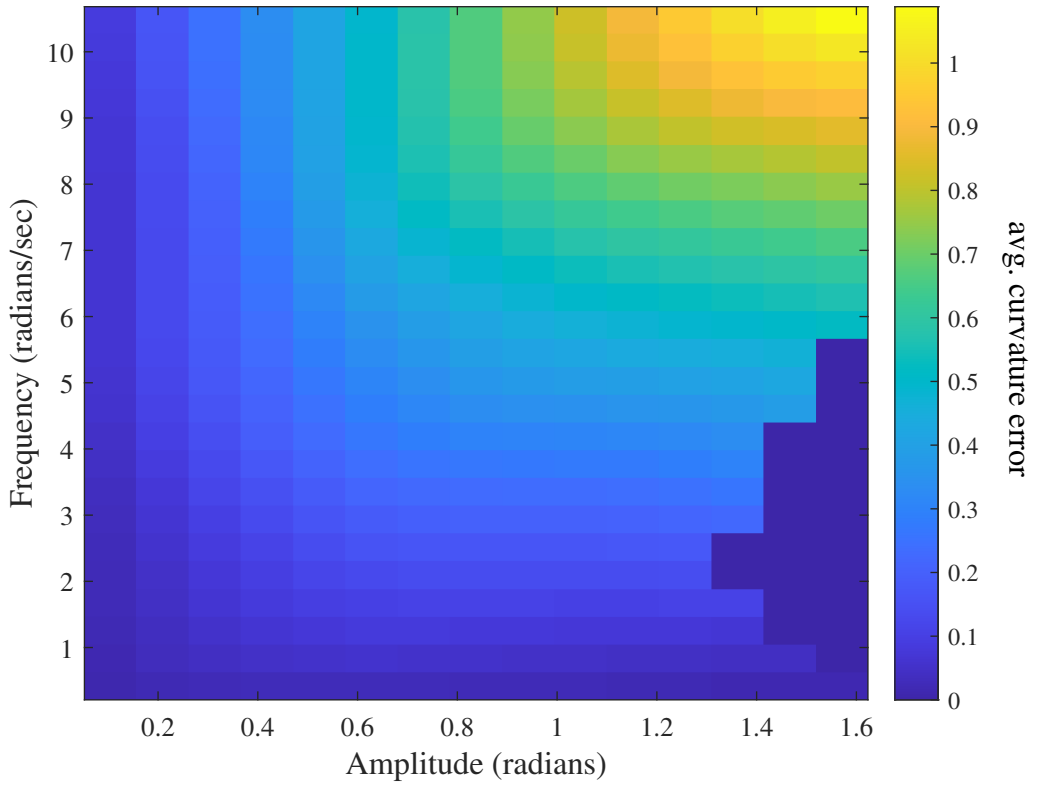

Figure 4.4: Open-loop error at a constant bending stiffness of $1.87 \times 10^4 Pa$

can see that at high frequency and/or amplitude, the average curvature error is high. This is undesirable because it leads to error in the direction of locomotion.

The average power loss due to friction is a key metric. miniature soft robots are severe energy constrained mostly due to the size of the robot. Hence, it is crucial that the robots spend the limited energy efficiently. At higher frequency and amplitude of the travelling wave, the average power lost to friction is observed to be higher figure 4.5.

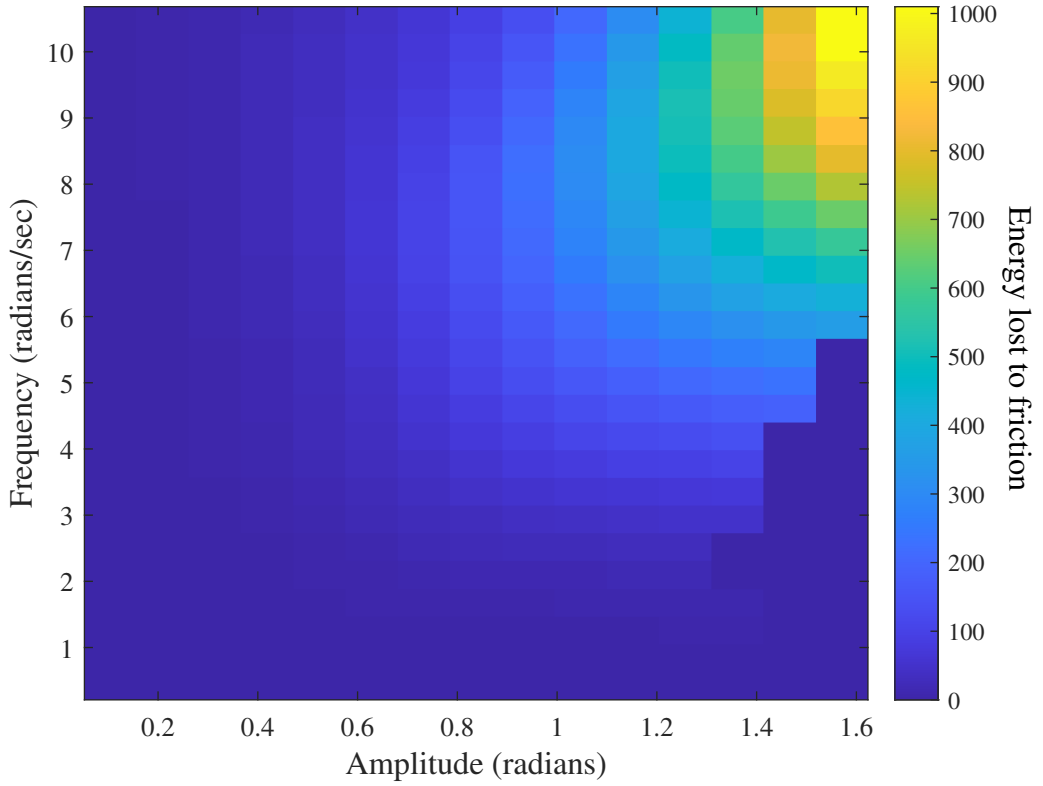

Figure 4.5: Open-loop energy loss due to fluid friction at a constant bending stiffness of $1.87 \times 10^4 Pa$

Therefore, a trade-off between the speed of swimming and the energy efficiency is the recommended plan of action. Based on the application and specifications of the robot, the open loop parameter study can be used identify the optimal values of frequency and amplitude of the travelling wave.

The bending stiffness of the soft-material is the next parameter analysed. The nature and the structure of the soft material influences the bending stiffness. Consequently, by design, we can make the stiffness a function of the direction of bending. For simplicity, it is assumed that the bio-inspired robot has the same bending stiffness in either direction of bending.

With increasing stiffness, the the soft-robot is observed to swim faster. We also

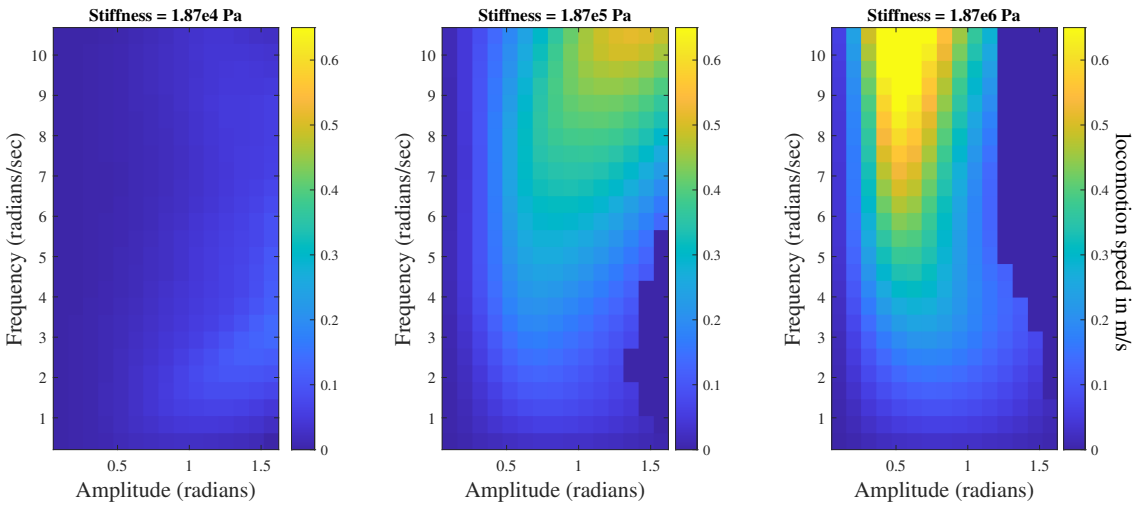

Figure 4.6: Open-loop average speed (m/s) at varying stiffness values

observe that at higher stiffness, the energy loss due to friction is reduced.

Developing a soft-robot with very high stiffness values overshadows the advantages of the "softness" of the robot. Hence, we are presented with a scenario where the softness of the robot results in lower swimming speeds and swimming efficiency. Since flexibility is of key importance in a soft-robot, a closed-loop controller that optimizes the swimming speed and swimming efficiency at low bending stiffness is needed.

4.3 Closed-loop dynamics and control

Though an open-loop controller proved to be sufficient to perform locomotion, major drawbacks in curvature error and energy efficiency indicate a need for a closed loop controller. Generally, in miniature soft-robots, the speed of locomotion is not the primary metric of interest. The operational longevity of the robot is primarily dictated by its locomotion efficiency.

The feedback controller is based of the actual curvature feedback controller presented

in section 3.2. The controller uses the measurements of actual curvature at each node and a decentralized algorithm to estimate the phase at each node.

The expression for the PID control input at each node is

$$u_i = \dot{\kappa}_{i,des}(t) + K_p e_i(t) + K_d \dot{e}_i(t) + K_i \int_0^t e_i(\tau) d\tau, \tag{4.3}$$

where $e_i = \kappa_{i,des} - \kappa_i$ is the error in actual curvature at node i.

4.4 Performance analysis

This section compares the open-loop and closed-loop performance. Firstly, we look at average speed of locomotion. From Figure 4.7, it is evident that the closed loop algorithm improves the locomotion speed of the soft segmented robot at a fixed stiffness level. The closed-loop controller ensures that the actual curvature of the soft-segmented robot. The feedback controller adjusts the rate of change of intrinsic curvature which is, in turn, the input to the system.

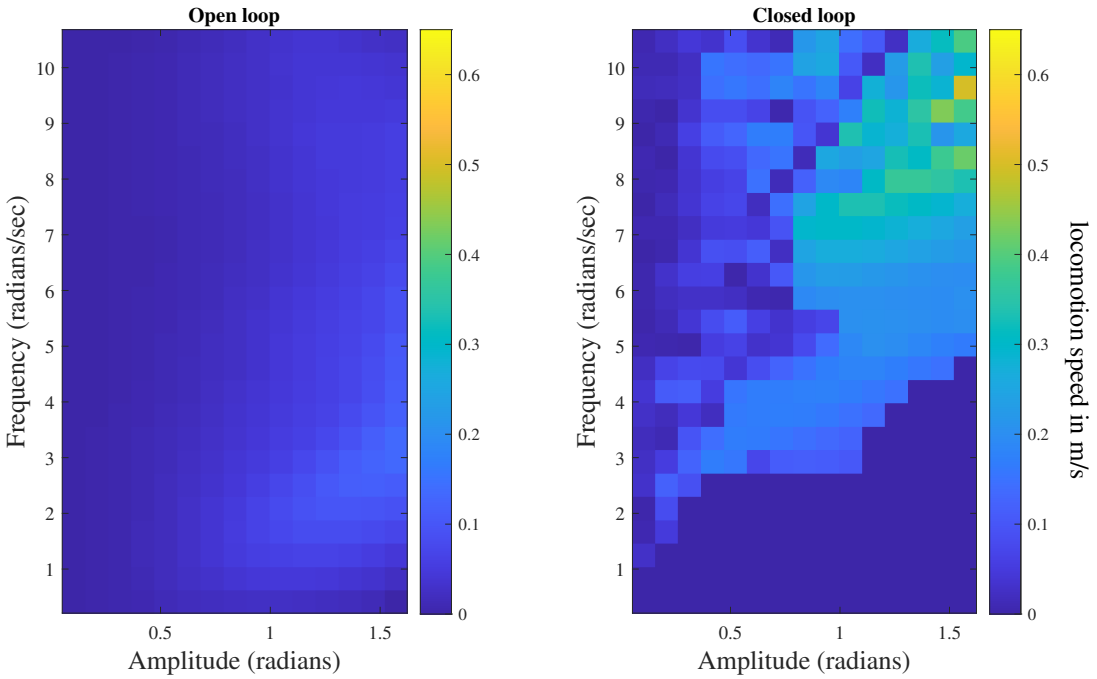

Figure 4.7: Open-loop speed vs closed-loop speed at a constant bending stiffness of $1.87 \times 10^4 Pa$

In the previous section, we defined the curvature error as a key metric of interest. We expect the closed-loop controller to reduce the curvature error. Figure 4.8 supports the above statement. In specific regions of the amplitude-frequency map, we observe considerable reduction in the curvature error.

Finally, we look at the energy lost due to friction. It is expected that the closed-loop system expends more energy to overcome fluid friction.

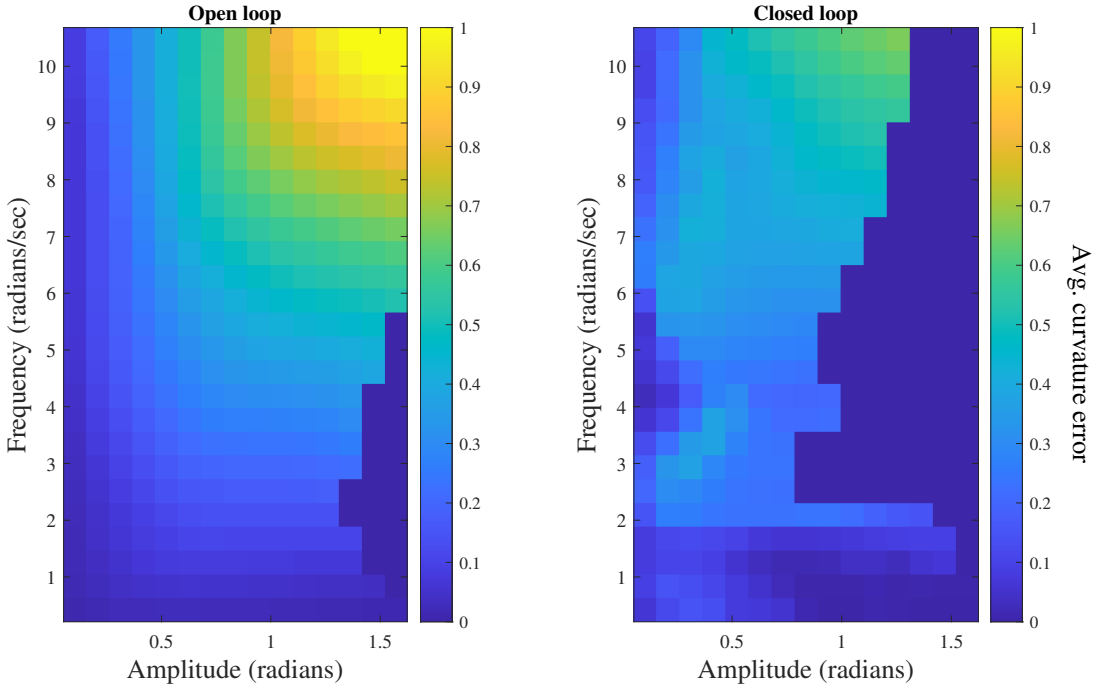

Figure 4.8: Open-loop curvature error vs closed-loop curvature error at a constant bending stiffness of $1.87 \times 10^4 Pa$

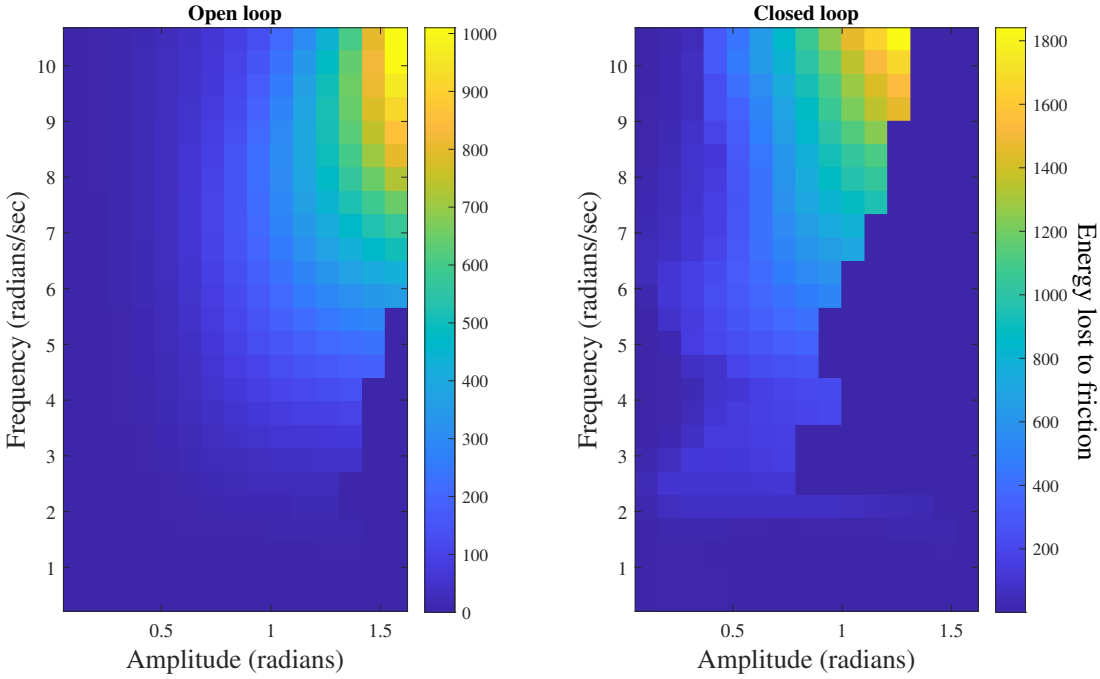

Figure 4.9: Open-loop vs closed-loop energy loss due to friction at a constant bending stiffness of $1.87 \times 10^4 Pa$

Chapter 5: Traveling-wave locomotion on land

This chapter explores terrestrial locomotion of soft segmented robots. To move on land, the robot needs to interact with the surface and nature of this interaction is defined by the surface friction. Broadly, there are two types of friction. Static friction is friction between two surfaces in contact that are not moving relative to each other. An object needs to over come this resistance in order to move. Kinetic friction on the other hand, occurs between two surfaces that are moving relative to each other. This dynamic friction results in a resistive force acting in a direction opposing the direction of movement. In the absence of friction, locomotion is impossible. Hence, by modeling frictional forces we can create a model to simulate terrestrial locomotion. We use the stick-slip model from Section 2.2.2 as the fundamental friction model in this chapter.

In nature, we see different terrestrial locomotion mechanisms. In the soft flexible domain, variations of worm-like inching and snake-like slithering are frequently observed. The focus of this chapter will be on worm-like slithering motion. The soft segmented robot is capable of shortening and elongating the length of its segments and in turn produce locomotion.

The structure of this chapter closely follows the previous chapter. First we understand the equations of motion that govern the robot. Then we simulate the open-loop dynamics

and compare them to the closed-loop performance of the robot.

5.1 Equations of motion

We combine the PDER state space model and the friction force model from section 2to arrive at the equations of motion that govern the dynamics of the soft segmented robot.

$$
\begin{aligned}
\dot{\boldsymbol{q}} &= \boldsymbol{v} \\
\dot{\boldsymbol{v}} &= -M^{-1}\left(\frac{\partial E_t}{\partial \boldsymbol{q}} + \boldsymbol{F}^{fr}\right) \\
\dot{\tilde{\boldsymbol{\kappa}}} &= B_\kappa \boldsymbol{u}_\kappa \\
\dot{\tilde{\boldsymbol{l}}} &= B_l \boldsymbol{u}_l,
\end{aligned}
\tag{5.1}
$$

In equation 5.1, the term $\boldsymbol{F}^{fr}$ captures the frictional force produced during locomotion. The magnitude and direction of the force is based on the algorithm illustrated in Figure 2.4.

5.2 Open-loop dynamics

Worm-like inching motion in soft segmented robots can be achieved by a traveling wave propagating through the body. This wave can either be a compression wave or an expansion wave. In nature, we observe that, inching worms demonstrate a compression wave moving from the tail to the head. In this section, we simulate a similar compression wave with the aim to produce locomotion.

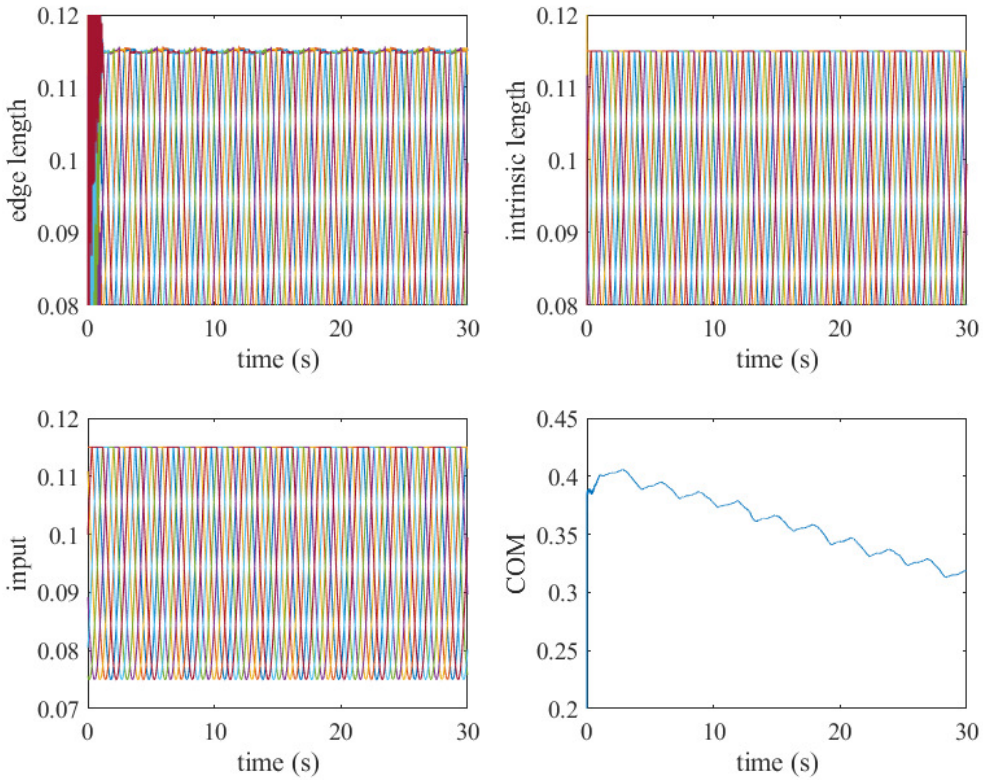

Figure 5.1: Open-loop simulation of inching motion. The plot of the COM shows the inching motion of the worm. $\mu_s = 1.15$ and $\mu_d = 0.8$

Figure 5.1 is a proof of concept. The soft segmented robot can successfully move by inching by interacting with the surface. We further examine two key factors which affect this locomotion: the static friction coefficient μ_s and the dynamic friction coefficient μ_d.

We observe that, with increasing static friction, the worm travels further. On the contrary, a lower dynamic friction coefficient results in better locomotion. Though Figure 5.2 shows a clear optimal performance region, it does not provide the complete picture. As discussed before, energy is a key metric in miniature soft robots. We need to analyse the energy that is needed to overcome friction and perform locomotion.

From Figure 5.3, it is clear that further locomotion comes at the cost of higher energy expenditure.

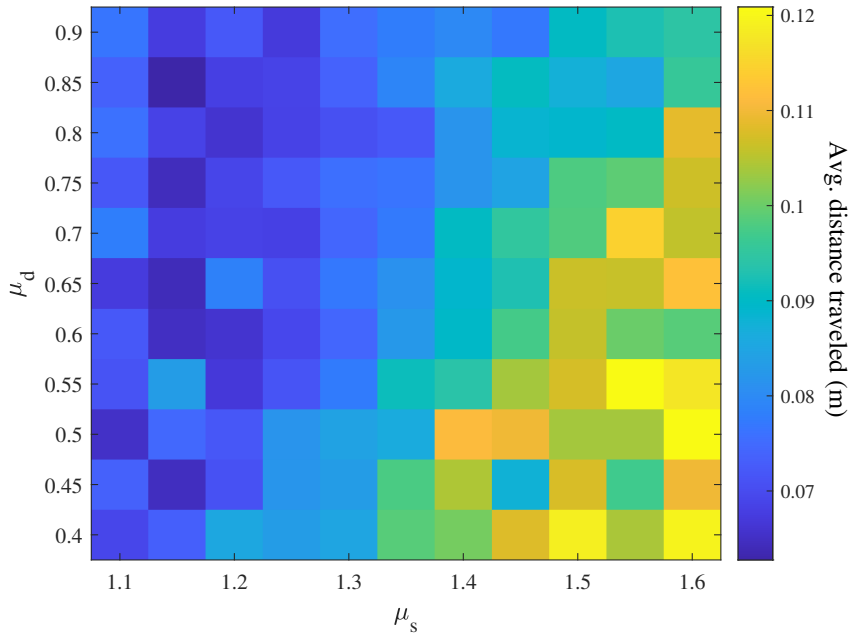

Figure 5.2: Open-loop simulation of inching motion for a range of μ_s and μ_d values. The plot represents the distance traveled in m

5.3 Closed loop dynamics and control

The feedback controller is based of the actual curvature feedback controller presented in section 3.2. The controller uses the measurements of actual curvature at each node and a decentralized algorithm to estimate the phase at each node. The expression for the control input at each node is-

$$u_i = \dot{\kappa}_{i,des}(t) + K_p e_i(t), \tag{5.2}$$

where $e_i = \kappa_{i,des} - \kappa_i$ is the error in actual curvature at node i.

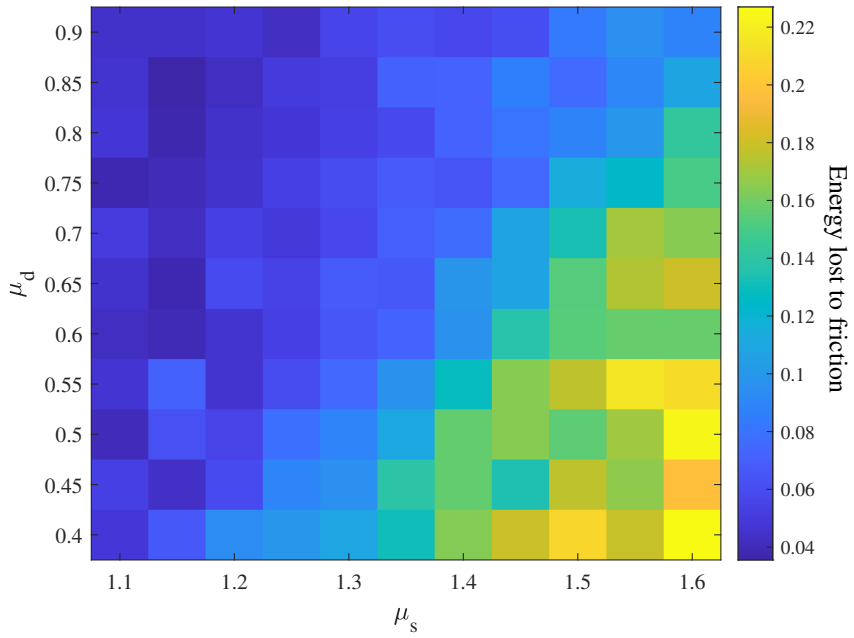

Figure 5.3: Open-loop simulation of inching motion for a range of μ_s and μ_d values. The plot represents the energy (J) spent to overcome friction

5.4 Performance analysis

Next we compare the performance of the open-loop and closed-loop controllers. The key metric of interest are locomotion distance and energy spent to overcome friction.

From Figure 5.4 we observe that the closed loop controller is clearly superior in terms of distance travelled in unite time. The controller performs exceptionally well even for large μ_d values. To fully understand the cost of this improvement, we now contrast the energy spent to overcome friction in each case.

From figure 5.4 we observe that this rise in locomotion performance comes at the cost of higher energy dissipation. This is an expected result and a necessary evil to improve locomotion performance.

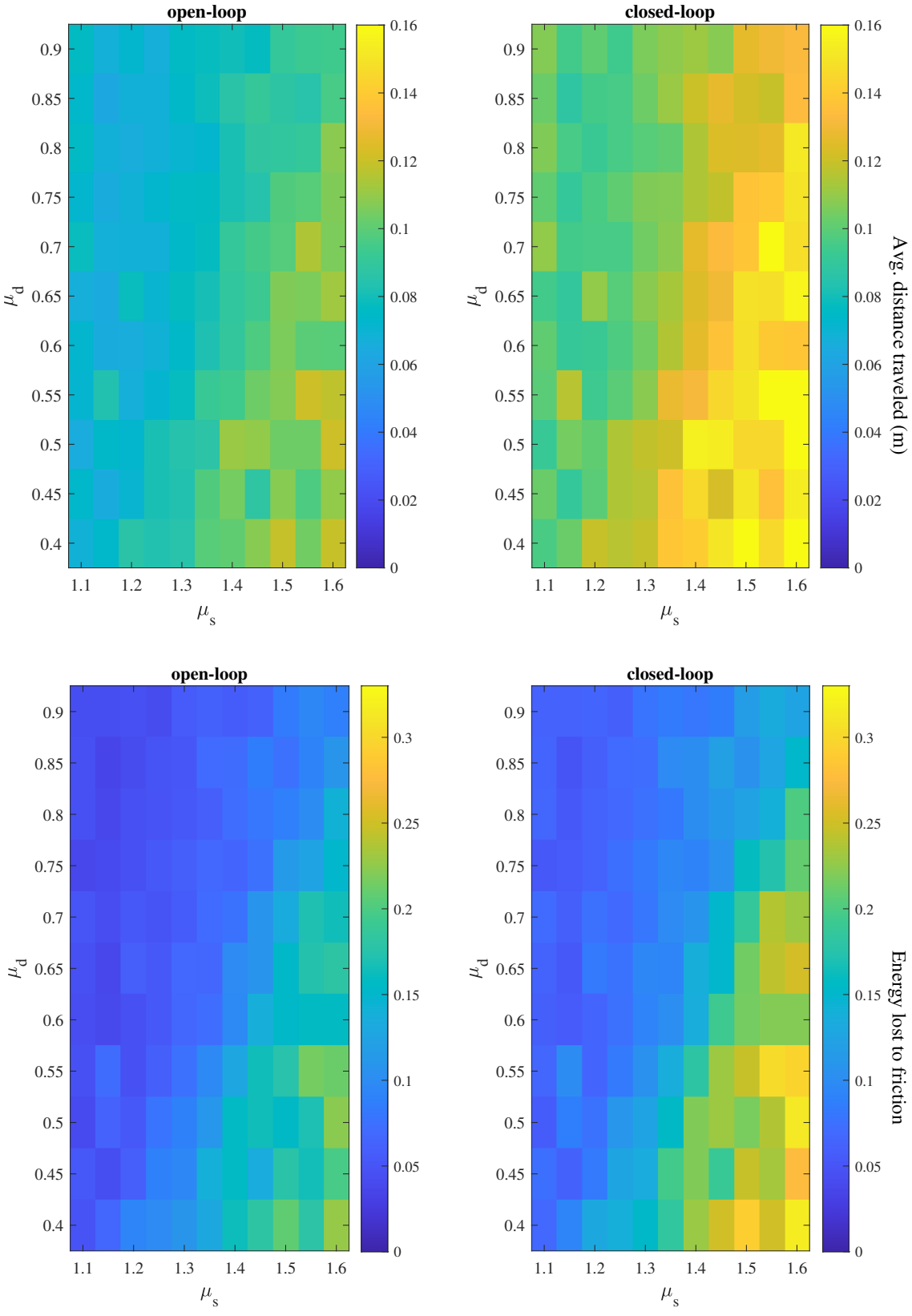

Figure 5.4: Open-loop vs closed-loop simulation of inching motion for a range of μ_s and μ_d values comparing the distance traveled and energy spent to overcome friction.

Chapter 6: Conclusion

Over the last few decades, engineering design has actively drawn inspiration from biological life. With advancements in non-traditional manufacturing technologies, realizing complex geometries has never been easier. This thesis investigates the performance of one such bio-inspired engineering solution. Compared to their rigid counterparts, soft segmented robots have decreased weight, size, and mechanical complexity. However, these flexible systems are highly non-linear and hence can be difficult to model. This combination of design flexibility and structural complexity makes the design and control of soft segmented robots a rich problem to be solved.

6.1 Summary of contributions

The primary contribution of this work is the mathematical model for feedback control of traveling-wave locomotion in underwater and terrestrial domains. The Planar Discrete Elastic Rod (PDER) framework results in an attractive and numerically efficient model that includes external forces and user inputs. A computationally tractable fluid force model is used to capture the influence of external environment. The proposed framework models both the added mass and inertial fluid forces acting on each soft segment in a fluid. (The work on underwater locomotion of soft segmented robot was previously published

as part of [2].)

The work on terrestrial locomotion incorporates a stick-slip friction model. Similar to the underwater case, the PDER framework is used to describe the dynamics of the system, now including frictional force from the stick-slip model. By modeling both static and dynamic friction, a computationally viable and physically accurate mathematical description of surface friction is proposed.

This work proposes a feedback-control algorithm based on a travelling wave to control the states of the soft segmented robot. An open-loop parameter study serves as the baseline against which the closed-loop performance is compared. The control strategy is decentralized, i.e, each segment can only interact with its neighboring nodes. Hence, the control law is computationally efficient, and impose fewer sensing and communication requirements that a centralized model.

The performance of the soft-segmented robot is dependent on various physical and control variables. An extensive parameter study is done to quantify the dependence of the performance metrics on these factors. This parameter study is intended to be used as a look-up table for future design changes or new developments in similar soft segmented robots.

6.2 Ongoing and future work

In future work we would suggest expanding the the underwater dynamics to include both stretching and bending modes. Superposition of both the modes can lead to interesting results and is an area worth exploring. Regarding the traveling wave, other wave schemes with possible phase offsets are observed to produce a turning motion. There is benefit in exploring novel wave schemes and feedback control methods. The controller developed in this thesis is a low level controller capable of tracking the required curvature. The closed-loop dynamics of the soft segmented robot can be used to develop a motion planning algorithm to help navigate the robot through a complex path.

Bibliography

[1] Nathaniel N. Goldberg, Xiaonan Huang, Carmel Majidi, Alyssa Novelia, Oliver M. O'Reilly, Derek A. Paley, and William L. Scott. On planar discrete elastic rod models for the locomotion of soft robots. *Soft Robotics*, 6(5):595–610, 2019.

[2] William L. Scott, Prateek Jaya Prakash, and Derek A. Paley. *Distributed Control of a Planar Discrete Elastic Rod for Eel-Inspired Underwater Locomotion*, pages 261–279. Springer International Publishing, Cham, 2021.

[3] Eleni Kelasidi, Pål Liljebäck, Kristin Y Pettersen, and Jan Tommy Gravdahl. Integral line-of-sight guidance for path following control of underwater snake robots: Theory and experiments. *IEEE Transactions on Robotics*, 33(3):610–628, 2017.

[4] Eleni Kelasidi, Pål Liljebäck, Kristin Y Pettersen, and Jan T Gravdahl. Experimental investigation of efficient locomotion of underwater snake robots for lateral undulation and eel-like motion patterns. *Robotics and Biomimetics*, 2(1):8, Dec 2015.

[5] Federico Renda, Francesco Giorgio-Serchi, Frederic Boyer, Cecilia Laschi, Jorge Dias, and Lakmal Seneviratne. A unified multi-soft-body dynamic model for underwater soft robots. *The International Journal of Robotics Research*, 37(6):648–666, 2018.

[6] Z.Y. Bayraktaroglu. Snake-like locomotion: Experimentations with a biologically inspired wheel-less snake robot. *Mechanism and Machine Theory*, 44(3):591 – 602, 2009. Special Issue on Bio-Inspired Mechanism Engineering.

[7] Frédéric Boyer, Mathieu Porez, and Wisama Khalil. Macro-continuous computed torque algorithm for a three-dimensional eel-like robot. *IEEE Transactions on Robotics*, 22(4):763–775, 2006.

[8] Caleb Christianson, Nathaniel N. Goldberg, Dimitri D. Deheyn, Shengqiang Cai, and Michael T. Tolley. Translucent soft robots driven by frameless fluid electrode dielectric elastomer actuators. *Science Robotics*, 3(17), 2018.

[9] Hui Feng, Yi Sun, Peter A. Todd, and Heow Pueh Lee. Body wave generation for anguilliform locomotion using a fiber-reinforced soft fluidic elastomer actuator array toward the development of the eel-inspired underwater soft robot. *Soft Robotics*, 7(2):233–250, 2020.

[10] Perrin E Schiebel, Jennifer M Rieser, Alex M Hubbard, Lillian Chen, D Zeb Rocklin, and Daniel I Goldman. Mechanical diffraction reveals the role of passive dynamics in a slithering snake. *Proceedings of the National Academy of Sciences*, 116(11):4798–4803, 2019.

[11] Colm McCaffrey, Takuya Umedachi, Weiwei Jiang, Takuya Sasatani, Yoshiaki Narusue, Ryuma Niiyama, and Yoshihiro Kawahara. Continuum robotic caterpillar with wirelessly powered shape memory alloy actuators. *Soft Robotics, available online ahead of print*, 2020.

[12] Zhijian Wang, Kai Li, Qiguang He, and Shengqiang Cai. A light-powered ultralight tensegrity robot with high deformability and load capacity. *Advanced Materials*, 31(7):1806849, 2019.

[13] Michael Wehner, Ryan L Truby, Daniel J Fitzgerald, Bobak Mosadegh, George M Whitesides, Jennifer A Lewis, and Robert J Wood. An integrated design and fabrication strategy for entirely soft, autonomous robots. *Nature*, 536(7617):451–455, 2016.

[14] James Gray and H. W. Lissmann. The kinetics of locomotion of the grass-snake. 1950.

[15] H. W. LISSMANN. Rectilinear locomotion in a snake (boa occidentalis). *Journal of Experimental Biology*, 26(4):368–379, 1950.

[16] B. C. Jayne. Muscular mechanisms of snake locomotion: an electromyographic study of the sidewinding and concertina modes of crotalus cerastes, nerodia fasciata and elaphe obsoleta. *Journal of Experimental Biology*, 140(1):1–33, 1988.

[17] Bruce C. Jayne. Kinematics of terrestrial snake locomotion. *Copeia*, 1986(4):915–927, 1986.

[18] Shigeo Hirose. *Biologically-inspired Robots: Snake-like locomotors and manipulators*. Oxford University Press, 1993.

[19] M. Sato, M. Fukaya, and T. Iwasaki. Serpentine locomotion with robotic snakes. *IEEE Control Systems Magazine*, 22(1):64–81, Feb 2002.

[20] Kenneth A McIsaac and James P Ostrowski. Motion planning for anguilliform locomotion. *IEEE Transactions on Robotics and Automation*, 19(4):637–652, 2003.

[21] Miklós Bergou, Max Wardetzky, Stephen Robinson, Basile Audoly, and Eitan Grinspun. Discrete elastic rods. *ACM Transactions on Graphics*, 27(3):63, 2008.

[22] M Khalid Jawed, Alyssa Novelia, and Oliver M O'Reilly. *A Primer on the Kinematics of Discrete Elastic Rods*. Springer, 2018.

[23] E. Kelasidi, K. Y. Pettersen, J. T. Gravdahl, and P. Liljebäck. Modeling of underwater snake robots. In *IEEE International Conference on Robotics and Automation (ICRA)*, pages 4540–4547, May 2014.

[24] JR Morison, JW Johnson, SA Schaaf, et al. The force exerted by surface waves on piles. *Journal of Petroleum Technology*, 2(05):149–154, 1950.

[25] Kevin C. Galloway, Kaitlyn P. Becker, Brennan Phillips, Jordan Kirby, Stephen Licht, Dan Tchernov, Robert J. Wood, and David F. Gruber. Soft robotic grippers for biological sampling on deep reefs. *Soft Robotics*, 3(1):23–33, 2016.